



OPEN

Natural variability has dominated Atlantic Meridional Overturning Circulation since 1900

Mojib Latif ^{1,2} ✉, Jing Sun ¹ ✉, Martin Visbeck ^{1,2} and M. Hadi Bordbar ³

There is debate about slowing of the Atlantic Meridional Overturning Circulation (AMOC), a key component of the global climate system. Some focus is on the sea surface temperature (SST) slightly cooling in parts of the subpolar North Atlantic despite widespread ocean warming. Atlantic SST is influenced by the AMOC, especially on decadal timescales and beyond. The local cooling could thus reflect AMOC slowing and diminishing heat transport, consistent with climate model responses to rising atmospheric greenhouse gas concentrations. Here we show from Atlantic SST the prevalence of natural AMOC variability since 1900. This is consistent with historical climate model simulations for 1900–2014 predicting on average AMOC slowing of about 1 Sv at 30° N after 1980, which is within the range of internal multidecadal variability derived from the models' preindustrial control runs. These results highlight the importance of systematic and sustained in-situ monitoring systems that can detect and attribute with high confidence an anthropogenic AMOC signal.

Global surface warming (global warming hereafter) since the beginning of the twentieth century is unequivocal, and humans are the main cause through the emission of vast amounts of greenhouse gases (GHGs), especially carbon dioxide (CO₂)^{1–3}. The oceans have stored more than 90% of the heat trapped in the climate system caused by the accumulation of GHGs in the atmosphere, thereby contributing to sea-level rise and leading to more frequent and longer lasting marine heat waves⁴. Moreover, the oceans have taken up about one third of the total anthropogenic CO₂ emissions since the start of industrialization, causing ocean acidification⁵. Both ocean warming and acidification already have adverse consequences for marine ecosystems⁶. Some of the global warming impacts, however, unfold slowly in the ocean due to its large thermal and dynamical inertia. Examples are sea-level rise and the response of the Atlantic Meridional Overturning Circulation (AMOC), a three-dimensional system of currents in the Atlantic Ocean with global climatic relevance^{7–10}.

Climate models predict substantial AMOC slowing if atmospheric GHG concentrations continue to rise unabatedly^{11–14}. Substantial AMOC slowing would drive major climatic impacts such as shifting rainfall patterns on land¹⁵, accelerating regional sea-level rise^{16,17} and reducing oceanic CO₂ uptake. However, it is still unclear as to whether sustained AMOC slowing is underway^{18–22}. Direct ocean-circulation observation in the North Atlantic (NA) is limited^{9,23–27}. Inferences drawn about the AMOC's history from proxy data²⁸ or indices derived from other variables, which may provide information about the circulation's variability (for example, sea surface temperature (SST)^{21,29,30}, salinity³¹ or Labrador Sea convection³²), are subject to large uncertainties.

Atlantic SST

Pronounced decadal and longer timescale (hereafter, long-term) natural variability³² complicates the detection of anthropogenic signals over the NA sector. Further, the drivers of long-term climate variability are not well understood (for example, the causes of the Atlantic Multidecadal Oscillation/Variability (AMO/V), the leading mode of long-term NA-SST variability^{33–35}). Internal^{36,37} as well

as external^{38–40} mechanisms have been proposed to contribute to the AMO/V, and the mechanisms also differ greatly among climate models^{39,41–44}. Observations suggest that the SST contrast between the NA and South Atlantic, termed interhemispheric dipole⁴⁵, could be linked to the AMOC, which in turn is forced by the low-frequency portion of the North Atlantic Oscillation (NAO; Fig. 1d; Latif et al.¹⁹), the leading mode of the Northern Hemisphere's atmospheric winter-circulation variability⁴⁶. This link is supported by a number of climate models (for example, Delworth et al.⁴⁷). However, the relationships between AMO/V, AMOC and NAO are obscured by variable external forcing^{48–50}. Remote forcing, for example, from the Southern Ocean (Martin et al.⁵¹), may also impact the AMOC.

Ocean-circulation changes most prominently influence the SST on a sub-basin scale. The SST cooling in parts of the subpolar NA, which is referred to as the North Atlantic warming hole (NAWH; Extended Data Fig. 1a), may be an example and the consequence of GHG-induced AMOC slowing and diminishing related northward ocean heat transport^{52–54}. Other causes of the NAWH have been discussed too, for example, increased ocean heat transport out of the subpolar NA into higher latitudes⁵⁵. Moreover, the deep mixed layers in the NAWH (Extended Data Fig. 1b), indicating strong vertical heat exchange, would delay externally forced surface warming. Anthropogenic aerosols reducing net surface solar radiation could also counteract the surface warming in the extratropical NA³⁹.

The 1900–2019 SST averaged over the NAWH (small boxes in Figs. 2b and 3b) and obtained from two observational datasets (Methods) exhibits strong long-term variability (Fig. 1a). Two other indices (Fig. 1b,c), averaging the SST over larger areas of the NA (Methods), exhibit similar long-term variability. All three indices indicate a major multidecadal cooling trend during 1930–1970. The later part of the cooling trend has been discussed in Hodson et al.⁵⁶. They conclude that internal as well as external factors could have contributed to the cooling in the 1960s and early 1970s.

The SST in the NAWH (Fig. 1a) underwent a fast and strong warming in the 1990s and featured pronounced multiannual-to-decadal variability after 2000 without any obvious trend. The atmospheric CO₂ forcing (Fig. 1d) and net top-of-the-atmosphere effective

¹GEOMAR Helmholtz Centre for Ocean Research Kiel, Kiel, Germany. ²Christian-Albrechts University Kiel, Kiel, Germany. ³Leibniz-Institut für Ostseeforschung Warnemünde – IOW, Rostock, Germany. ✉e-mail: mlatif@geomar.de; jsun@geomar.de

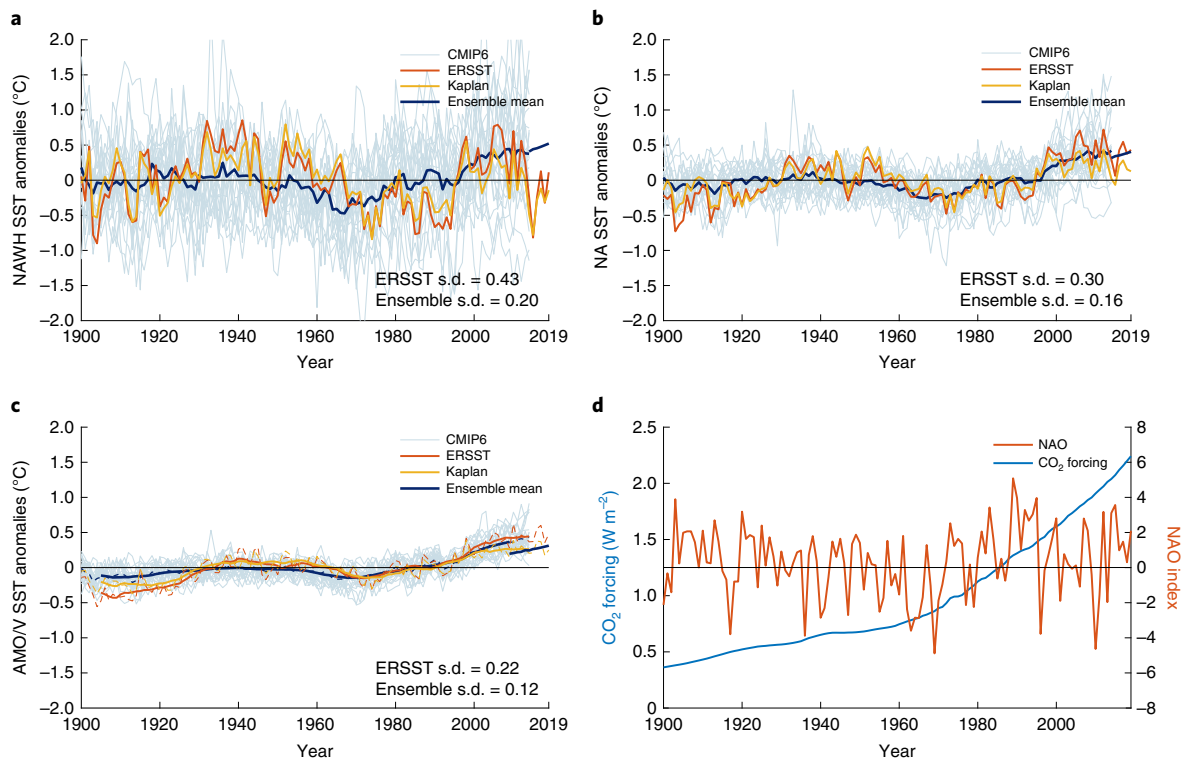


Fig. 1 | Time series of different SST indices. **a**, The NAWH SST index ($^{\circ}\text{C}$), defined as the annual SST anomalies averaged over the region 46°N – 62°N and 46°W – 20°W . Observations for 1900–2019 from ERSSTv.5 (orange) and Kaplan SST v.2 (yellow), and ensemble-mean SST for 1900–2014 (dark blue line) from the historical simulations with the CMIP6 models and the individual historical simulations (thin grey lines) are shown. **b**, Same as **a** but for the NA-SST index ($^{\circ}\text{C}$), defined as the annual SST anomalies averaged over the region 40°N – 60°N and 80°W – 0°E . **c**, Same as **a** but for the AMO/V ($^{\circ}\text{C}$) index, defined as the 11-year running mean of the annual SST anomalies averaged over the region 0°N – 65°N and 80°W – 0°E . The SST indices in **a–c** are calculated as area-weighted means. **d**, NAO index (dimensionless) for 1900–2019 (red), defined as the difference in the normalized winter (December–March) sea-level pressure between Lisbon (Portugal) and Stykkisholmur/Reykjavik (Iceland). The blue curve indicates the equivalent CO_2 radiative forcing (W m^{-2}) for 1900–2019, which is taken from the Representative Concentration Pathway (RCP) SSP5-8.5 after 2014.

radiative forcing (ERF; Methods and Figs. 2a and 3a), however, strongly increased from the 1970s onward. We note that the strong year-to-year variability in the SST of the NAWH is mostly due to atmospheric heat-flux forcing linked to the winter NAO⁵⁷. This short-term variability is not addressed here, as the focus of this study is on the long-term variability.

Spatial structure of long-term SST change

Empirical orthogonal function (EOF) analysis is applied to the observed annual SST anomalies (blue boxes in Figs. 2b and 3b; Methods), which is a variance-maximizing multivariate statistical technique⁵⁸. The two leading modes, EOF1 and EOF2, are dominated by long-term variability and are of interest here. EOF1 accounts for 52.2% of the total Atlantic SST variability. The time evolution (principal component) of EOF1, PC1 (Fig. 2a), is governed by an accelerating upward trend with substantial superimposed less-energetic interannual-to-multidecadal variability. PC1 follows the long-term evolution of the ERF well, with a correlation coefficient of 0.83 when the Shared Socioeconomic Pathway 5-8.5 (SSP5-8.5; Methods) scenario is considered during 2015–2019. We suggest that EOF1 describes the externally forced Atlantic SST variability, in particular the effects of global warming. The prominent, short-lived, downward spikes in the ERF during the second half of the twentieth century, however, are not well captured by PC1 and have been attributed to explosive volcanic eruptions⁵⁹.

The pattern of EOF1, shown as the local regression coefficients upon PC1 (Fig. 2b), exhibits positive anomalies over the Atlantic basin, with the exception of the NAWH. PC1 accounts for up to

80% of the SST variability in the tropical Atlantic but hardly any in the NAWH. In most other regions of the Atlantic, the explained variances amount to at least 50%. EOF1 explains a relatively large fraction of the SST variability over most of the global ocean. We note the warming hole in the subpolar Southern Ocean (Fig. 2b and Extended Data Fig. 1a); there, stronger westerly surface winds (associated with stratospheric ozone loss^{60,61}) or Antarctic meltwater⁶² may have offset GHG-forced warming. Moreover, in climate models, the internal long-term variability is particularly strong in both the Southern Ocean and NA^{63–67}, hindering detection of externally forced signals.

The second most energetic mode (EOF2; Fig. 3) accounts for 12.1% of the total Atlantic SST variability. The corresponding time series, PC2 (Fig. 3a), has no obvious relationship with the ERF and exhibits pronounced decadal-to-multidecadal variability but no trend. EOF2 is picking up the signal of the Atlantic interhemispheric dipole, which has been linked to long-term AMOC variability in climate models^{29,30,44,68–70}. Centres with opposite sign are observed in the subpolar NA and in the South Atlantic (Fig. 3b), where EOF2 typically accounts for up to 60% and 20% of the local SST variability, respectively. There is a highly significant correlation amounting to 0.7 between PC2 and an Atlantic interhemispheric dipole index as defined by Latif et al.¹⁹. EOF2 explains considerably less variance in the tropical Atlantic where EOF1 explains the most. The salient feature of PC2 (Fig. 3a) is the marked decline during 1930–1970. We note that the multidecadal decline in PC2 was preceded by a multidecadal decline in the winter NAO index (Extended Data Fig. 2). However, the largest significant correlation,

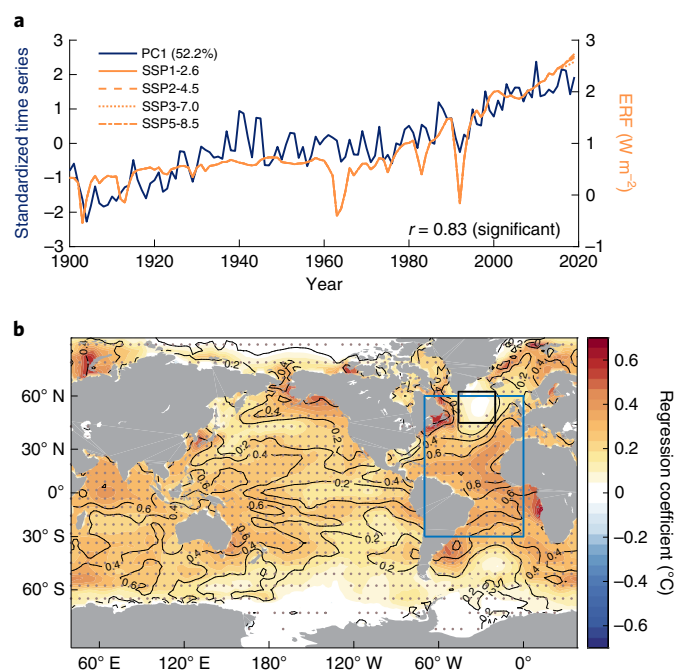


Fig. 2 | EOF1 time series and regression map. Leading EOF (EOF1) of Atlantic SST calculated from ERSSTv.5 over the period 1900–2019. **a**, The blue curve indicates the principal component time series (PC1) of EOF1. The orange curve indicates the historical ERF and the different RCP SSPs after 2014 (SSP1-2.6, SSP2-4.5, SSP3-7.0 and SSP5-8.5). The correlation coefficient (r) between the PC1 and SSP5-8.5 is 0.83, which is statistically significant at the 95% confidence level. **b**, Regression map of the observed SSTs upon PC1. Colour shading shows the coefficient of the regression. The contours denote the explained variance; the contour interval is 0.2. The dots indicate significance at the 95% level. The blue box indicates the region over which the EOF analysis was performed, and the black box marks the region over which the NAWH index (Fig. 1a) is defined.

which is negative, is observed with no lag (Extended Data Fig. 3). We hypothesize that EOF2 describes the internal, AMOC-related, SST variability in the Atlantic.

Historical climate model simulations

The observed NA-SST variability is within the range of the historical simulations with state-of-the-art climate models from the Coupled Model Intercomparison Project phase 6 (CMIP6; Methods and Fig. 1a–c), employing estimates of external forcing from 1900 to 2014 (ref. ⁷¹). A measure of the externally forced variability is given by the ensemble mean, that is, by averaging over all simulations. The ensemble-mean SST variability is much weaker than the observed variability in the NAWH (Fig. 1a) and subpolar NA (Fig. 1b), suggesting the prevalence of internal SST variability in these two regions. The observed SST variability is also underestimated by the ensemble mean (but to a lesser extent) when averaging over the whole NA (Fig. 1c), supporting a major role of external forcing in driving tropical and subtropical Atlantic SST. This is consistent with EOF1, which is closely linked to the ERF (Fig. 2a), explaining the most variance in the tropics and subtropics. The ensemble-mean NA SSTs lead the observed SSTs by about a decade in all three index regions (Fig. 1a–c). We note that historical external forcing is subject to considerable uncertainties. Aerosol–cloud interaction is the largest source of uncertainty in estimating historical anthropogenic radiative forcing, and representing this interaction in climate models poses a major challenge^{72,73}. Finally, in the regions of the three SST indices, the 40-year linear SST trend during 1975–2014 lies

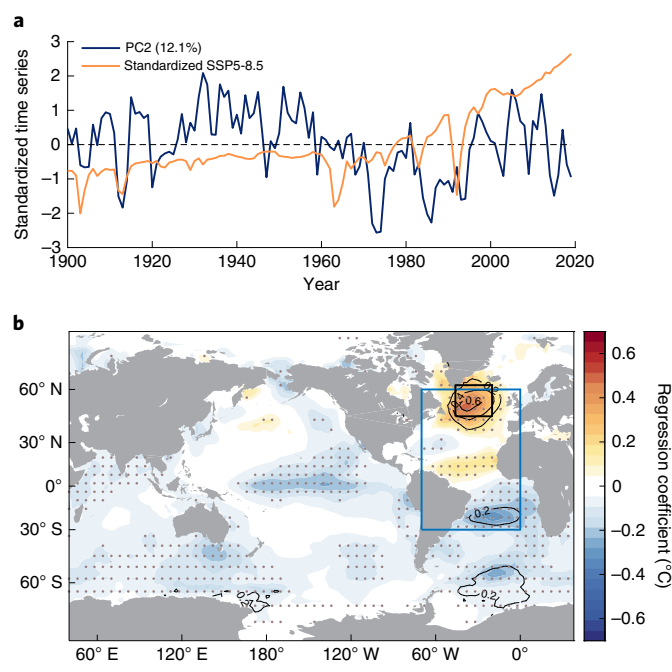


Fig. 3 | EOF2 time series and regression map. Second most energetic EOF (EOF2) of Atlantic SST calculated from ERSSTv.5 over the period 1900–2019. **a**, The blue curve indicates the principal component time series (PC2) of EOF2. The orange curve indicates the standardized RCP SSP5-8.5. **b**, Regression map of the observed SSTs upon PC2. Colour shading shows the coefficient of the regression. The contours denote the explained variance; the contour interval is 0.2. The dots indicate significance at the 95% level. The blue box indicates the region over which the EOF analysis was performed, and the black box marks the region over which the NAWH index (Fig. 1a) is defined.

within the trend distribution derived from the preindustrial control integrations of the models (Extended Data Fig. 4).

An EOF analysis is applied jointly to the ensemble-mean Atlantic SST and Atlantic meridional overturning streamfunction (MOC). The SST pattern (Fig. 4a) of the leading mode, EOF1_{mod}, accounting for 53.6% of the joint variance is similar to that of EOF1 (Fig. 2b), with major warming over most of the Atlantic and a warming hole in the subpolar NA south of Greenland. Variances in SST explained by EOF1_{mod} are generally large, exhibiting a maximum in the subtropical NA with values in localized regions exceeding 90%, and a minimum south of Greenland with values of less than 10% (Fig. 4a). The MOC pattern of EOF1_{mod} exhibits negative loadings north of the Equator, indicating weaker overturning, that are centred near 40°N in the depth range of 1,000–2,000 m (Fig. 4b). Positive loadings are observed south of the Equator. With regard to MOC, the explained variances are largest in the centre of the negative loadings, where they amount to about 80% (Fig. 4b). Regions of large explained variances indicate a high model consistency.

In climate models, MOC anomalies linked to changes in North Atlantic Deep Water formation first appear in the subpolar NA and then propagate southward⁷⁴. Fully developed AMOC slowing is characterized by basin-wide negative streamfunction anomalies in the models¹³. EOF1_{mod} is thus consistent with the initial stage of AMOC slowing. Because EOF1_{mod} is the leading mode of the externally forced variability in SST and MOC in the models, PC1_{mod} (Fig. 4c) is expected to be significantly correlated with the ERF. The correlation coefficient between the two time series amounts to 0.79. PC1_{mod} is governed by multidecadal variability until about 1980, and it exhibits a sustained upward trend thereafter. Since 1980, there is

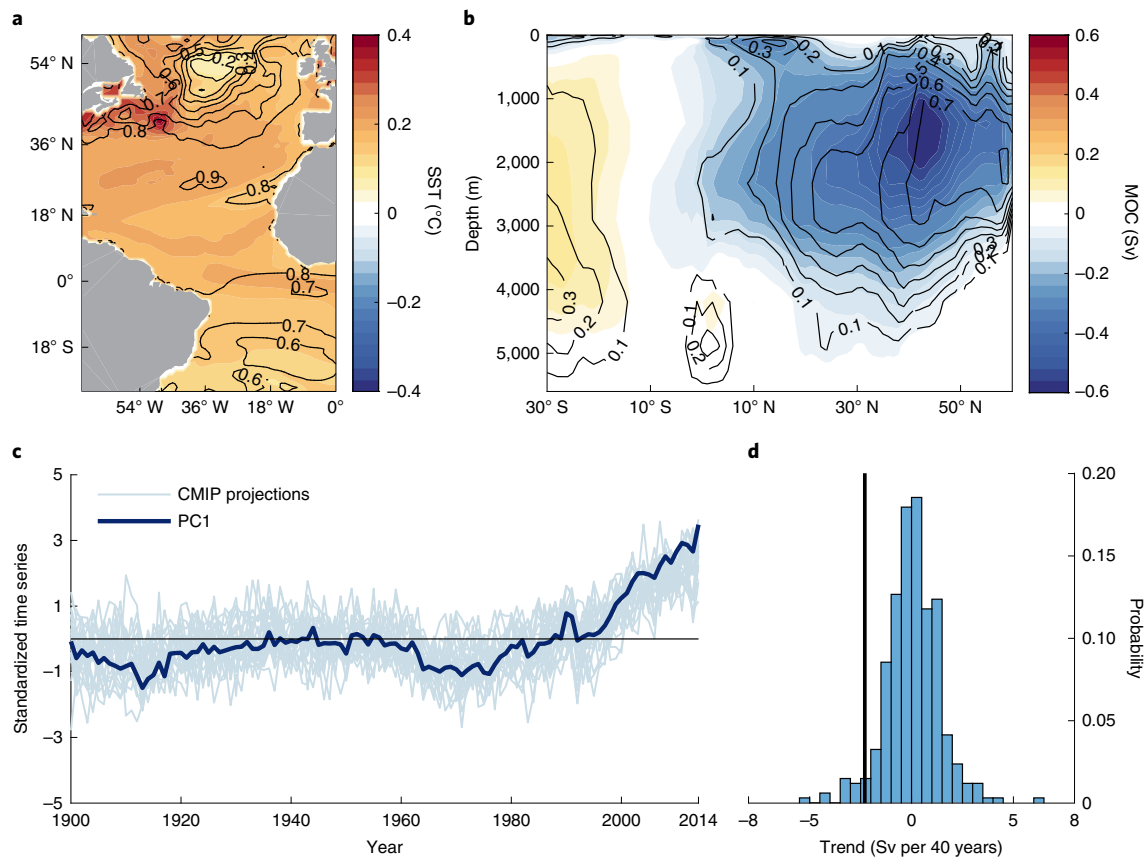


Fig. 4 | Joint EOF of SST and MOC of CMIP6 model ensemble mean. First joint EOF (EOF1_{mod}) of the ensemble-mean Atlantic SST and MOC, derived from the historical simulations with the CMIP6 models for 1900–2014. The ensemble mean is an estimate of the externally forced variability. **a–c**, SST pattern (**a**; °C), MOC pattern (**b**; Sv) and the principal component time series (PC1_{mod} , thick line) and projections of the individual climate models onto EOF1_{mod} (thin lines) (**c**). Contours in **a** and **b** denote explained variances (contour interval is 0.1) and colour shading indicates the corresponding spatial mode. EOF1_{mod} accounts for 53.6% of the joint variance. **d**, The probability distribution of non-overlapping 40-year trends (with an interval of 0.5 Sv per 40 years; blue bars), derived from the pre-industrial control integrations of the CMIP6 models. The vertical black line indicates the 40-year trend for 1975–2014 from the ensemble mean of CMIP6 historical simulations.

a reduction in the AMOC transport at 30°N that amounts to about 1 Sv ($10^6 \text{ m}^3 \text{ s}^{-1}$), which is assumed to be within the range of natural variability. This is supported by the distribution of non-overlapping 40-year MOC trends calculated from the preindustrial control integrations of the CMIP6 models (Fig. 4d), providing estimates of the internal MOC variability. The ensemble-mean reduction in ocean heat transport at 50°N is about 0.03 PW. We compare the AMOC index at 26.5°N reconstructed from EOF1_{mod} with the RAPID data⁷⁵ (Extended Data Fig. 1f). The 2004–2014 trend from RAPID amounts to -4.1 Sv and that from the reconstruction to -0.5 Sv. When assuming that the CMIP6-ensemble mean realistically represents the externally forced MOC variability, the trend from RAPID must contain a strong contribution from long-term internal variability. This is consistent with Weijer et al.¹¹, who analysed another subset of the CMIP6 models, reporting that linear trends over the entire 1850–2014 historical period are generally neutral.

Discussion

Observed SSTs and a large ensemble of historical simulations with state-of-the-art climate models suggest the prevalence of internal AMOC variability since the beginning of the twentieth century. Observations and individual model runs show comparable SST variability in the NAWH region. However, the models' ensemble-mean signal is much smaller, indicative of the prevalence of internal variability. Further, most of the SST cooling in the subpolar NA, which has been attributed to anthropogenic AMOC slowing²¹, occurred

during 1930–1970, when the radiative forcing did not exhibit a major upward trend. We conclude that the anthropogenic signal in the AMOC cannot be reliably estimated from observed SST. A linear and direct relationship between radiative forcing and AMOC may not exist. Further, the relevant physical processes could be shared across EOF modes, or a mode could represent more than one process.

A relatively stable AMOC and associated northward heat transport during the past decades is also supported by ocean syntheses combining ocean general circulation models and data^{76,77}, hindcasts with ocean general circulation models forced by observed atmospheric boundary conditions⁷⁸ and instrumental measurements of key AMOC components^{9,22,79–81}. Neither of these datasets suggest major AMOC slowing since 1980, and neither of the AMOC indices from Rahmstorf et al.²⁰ or Caesar et al.²¹ show an overall AMOC decline since 1980.

An important remaining issue is the question of how well the externally forced part of the Atlantic SSTs can be determined. Standard EOF analysis has been used above to identify the forced component. We additionally used two other methods. First, we applied principal oscillation pattern (POP) analysis (Methods) to the observed SSTs, again only over the Atlantic Ocean. The results of the POP analysis (Extended Data Fig. 5) are similar to those of the EOF analysis (Fig. 2), in that the time series of the leading POP mode (POP1) is highly correlated with the ERF ($r=0.85$; Extended Data Fig. 5a) and POP1 (Extended Data Fig. 5b) is similar to EOF1

(Fig. 2b). Second, we derived the externally forced component from the historical simulations with the CMIP6 models by applying signal-to-noise ratio (S/N) maximizing EOF analysis (Methods) to the modelled SSTs over the global ocean (Extended Data Fig. 6). As expected, the time series of the leading mode (S/N EOF1) is highly correlated with the ERF ($r=0.9$, Extended Data Fig. 6a). The associated regression pattern (Extended Data Fig. 6b) is similar to that linked to both EOF1 (Fig. 2b) and POP1 (Extended Data Fig. 5b), indicating little sensitivity to the choice of the statistical method in determining the externally forced SST variability.

We subtracted the variability associated with S/N-EOF1 from the observed SSTs to estimate the internal SST variability, and standard EOF analysis was applied to the residuals over the Atlantic. The second most energetic EOF mode (EOF2_{res}; Extended Data Fig. 7), accounting for 19.2% of the variability in the residuals, is multidecadal (Extended Data Fig. 7a). EOF2_{res} is the interhemispheric dipole, with explained variances up to 40% in the NAWH and in the centre of the southern pole (Extended Data Fig. 7b). EOF2_{res} is similar to EOF2 (Fig. 3), which is reassuring and supports the notion that EOF2 actually reflects internal SST variability.

The leading EOF of the residuals over the Atlantic (EOF1_{res}; Extended Data Fig. 8) accounts for 27.1% of the variance. Its time series (PC1_{res}) is characterized by a marked centennial change with a minimum in the 1940s (Extended Data Fig. 8a). Over the Atlantic, the regression coefficients upon PC1_{res} are largest north of the Equator (Extended Data Fig. 8b) and reminiscent of the “horseshoe” pattern linked to the positive phase of the NAO. PC1_{res} and the annual-mean NAO index exhibit a statistically significant correlation of 0.4.

A number of factors, internal and external, can influence the AMOC. Menary et al.³⁸ report that the multi-model mean AMOC strengthened by approximately 10% from 1850 to 1985 in historical simulations with CMIP5 and CMIP6 models, which has been attributed to aerosol forcing. This is consistent with our study in that the AMOC slowing largely takes place after 1980. Analysis of single-forcing experiments by Menary et al.³⁸ reveal that the forced response of the AMOC is a balance of opposing contributions from aerosols, increasing AMOC, and GHGs, decreasing AMOC. Besides surface heat flux, surface freshwater input from Greenland ice melt is thought to be an important factor causing anthropogenic AMOC slowing. Meltwater forcing is not considered in the historical simulations with the CMIP6 models, which may cause underestimation of AMOC slowing. A high-resolution ocean general circulation model study finds that the present meltwater forcing from the west Greenland Ice Sheet is not sufficiently large to drive significant reductions in North Atlantic Deep Water formation and thus AMOC strength⁸². Climate model sensitivity to external forcing, however, is a long-standing issue, also with regard to the AMOC's sensitivity to freshwater forcing⁸³. In summary, our results reinforce the need for systematic and sustained in-situ AMOC observation systems to detect with high confidence externally forced AMOC slowing^{9,84,75}.

Online content

Any methods, additional references, Nature Research reporting summaries, source data, extended data, supplementary information, acknowledgements, peer review information; details of author contributions and competing interests; and statements of data and code availability are available at <https://doi.org/10.1038/s41558-022-01342-4>.

Received: 25 April 2021; Accepted: 9 March 2022;
Published online: 25 April 2022

References

- IPCC *Climate Change 2013: The Physical Science Basis* (eds Stocker, T. F. et al.) (Cambridge Univ. Press, 2013); <https://doi.org/10.1017/CBO9781107415324>
- IPCC *Climate Change 2014: Synthesis Report* (eds Core Writing Team, Pachauri, R. K. & Meyer, L. A.) (IPCC, 2014).
- IPCC: Summary for Policymakers. In *Climate Change 2021: The Physical Science Basis* (eds Masson-Delmotte, V. et al.) (Cambridge Univ. Press, in the press).
- Oliver, E. C. J. et al. Longer and more frequent marine heatwaves over the past century. *Nat. Commun.* **9**, 1324 (2018).
- Dupont, S. & Pörtner, H. Get ready for ocean acidification. *Nature* **498**, 429 (2013).
- Bindoff, N. L. et al. in *Special Report on the Ocean and Cryosphere in a Changing Climate* (eds Pörtner, H.-O. et al.) Ch. 5 (Cambridge Univ. Press, 2019).
- Broecker, W. The great ocean conveyor. *Oceanography* **4**, 79–89 (1991).
- Srokosz, M. et al. Past, present, and future changes in the Atlantic Meridional Overturning Circulation. *Bull. Am. Meteorol. Soc.* **93**, 1663–1676 (2012).
- Frajka-Williams, E. et al. Atlantic Meridional Overturning Circulation: observed transport and variability. *Front. Mar. Sci.* <https://doi.org/10.3389/fmars.2019.00260> (2019).
- Zhang, R. et al. A review of the role of the Atlantic Meridional Overturning Circulation in Atlantic multidecadal variability and associated climate impacts. *Rev. Geophys.* **57**, 316–375 (2019).
- Weijer, W., Cheng, W., Garuba, O. A., Hu, A. & Nadiga, B. T. CMIP6 models predict significant 21st century decline of the Atlantic Meridional Overturning Circulation. *Geophys. Res. Lett.* <https://doi.org/10.1029/2019GL086075> (2020).
- Menary, M. B. & Wood, R. A. An anatomy of the projected North Atlantic warming hole in CMIP5 models. *Clim. Dyn.* **50**, 3063–3080 (2018).
- Reintges, A., Martin, T., Latif, M. & Keenlyside, N. S. Uncertainty in twenty-first century projections of the Atlantic Meridional Overturning Circulation in CMIP3 and CMIP5 models. *Clim. Dyn.* **49**, 1495–1511 (2017).
- Schmittner, A., Latif, M. & Schneider, B. Model projections of the North Atlantic thermohaline circulation for the 21st century assessed by observations. *Geophys. Res. Lett.* **32**, L23710 (2005).
- Liu, W., Fedorov, A. V., Xie, S.-P. & Hu, S. Climate impacts of a weakened Atlantic Meridional Overturning Circulation in a warming climate. *Sci. Adv.* <https://doi.org/10.1126/sciadv.aaz4876> (2020).
- Levermann, A., Griesel, A., Hofmann, M., Montoya, M. & Rahmstorf, S. Dynamic sea level changes following changes in the thermohaline circulation. *Clim. Dyn.* **24**, 347–354 (2005).
- Landerer, F. W., Jungclaus, J. H. & Marotzke, J. Regional dynamic and steric sea level change in response to the IPCC-A1B scenario. *J. Phys. Oceanogr.* **37**, 296–312 (2007).
- Bryden, H. L., Longworth, H. R. & Cunningham, S. A. Slowing of the Atlantic Meridional Overturning Circulation at 25°N. *Nature* **438**, 655–657 (2005).
- Latif, M. et al. Is the thermohaline circulation changing? *J. Clim.* **19**, 4631–4637 (2006).
- Rahmstorf, S. et al. Exceptional twentieth-century slowdown in Atlantic Ocean overturning circulation. *Nat. Clim. Change* **5**, 475–480 (2015).
- Caesar, L., Rahmstorf, S., Robinson, A., Feulner, G. & Saba, V. Observed fingerprint of a weakening Atlantic Ocean overturning circulation. *Nature* **556**, 191–196 (2018).
- Fu, Y., Li, F., Karstensen, J. & Wang, C. A stable Atlantic Meridional Overturning Circulation in a changing North Atlantic Ocean since the 1990s. *Sci. Adv.* <https://doi.org/10.1126/sciadv.abc7836> (2020).
- Cunningham, S. A. et al. Temporal variability of the Atlantic Meridional Overturning Circulation at 26.5°N. *Science* **317**, 935–938 (2007).
- Srokosz, M. A. & Bryden, H. L. Observing the Atlantic Meridional Overturning Circulation yields a decade of inevitable surprises. *Science* <https://doi.org/10.1126/science.1255575> (2015).
- Toole, J. M., Andres, M., Le Bras, I. A., Joyce, T. M. & McCartney, M. S. Moored observations of the Deep Western Boundary Current in the NW Atlantic: 2004–2014. *J. Geophys. Res. Oceans* **122**, 7488–7505 (2017).
- Handmann, P. et al. The Deep Western Boundary Current in the Labrador Sea from observations and a high-resolution model. *J. Geophys. Res. Oceans* **123**, 2829–2850 (2018).
- Lobelle, D., Beaulieu, C., Livina, V., Sévellec, F. & Frajka-Williams, E. Detectability of an AMOC decline in current and projected climate changes. *Geophys. Res. Lett.* <https://doi.org/10.1029/2020GL089974> (2020).
- Caesar, L., McCarthy, G. D., Thornalley, D. J. R., Cahill, N. & Rahmstorf, S. Current Atlantic Meridional Overturning Circulation weakest in last millennium. *Nat. Geosci.* **14**, 118–120 (2021).
- Latif, M. et al. Reconstructing, monitoring, and predicting multidecadal-scale changes in the North Atlantic thermohaline circulation with sea surface temperature. *J. Clim.* **17**, 1605–1614 (2004).
- Dima, M. & Lohmann, G. Evidence for two distinct modes of large-scale ocean circulation changes over the last century. *J. Clim.* **23**, 5–16 (2010).
- Zhu, C. & Liu, Z. Weakening Atlantic overturning circulation causes South Atlantic salinity pile-up. *Nat. Clim. Change* **10**, 998–1003 (2020).

32. Thornalley, D. J. R. et al. Anomalously weak Labrador Sea convection and Atlantic overturning during the past 150 years. *Nature* **556**, 227–230 (2018).
33. Knight, J. R. A signature of persistent natural thermohaline circulation cycles in observed climate. *Geophys. Res. Lett.* **32**, L20708 (2005).
34. Sutton, R. T. & Hodson, D. L. R. Atlantic Ocean forcing of North American and European summer climate. *Science* **309**, 115–118 (2005).
35. Zhang, R. & Delworth, T. L. Impact of Atlantic multidecadal oscillations on India/Sahel rainfall and Atlantic hurricanes. *Geophys. Res. Lett.* **33**, L17712 (2006).
36. Ting, M., Kushnir, Y., Seager, R. & Li, C. Forced and internal twentieth-century SST trends in the North Atlantic. *J. Clim.* **22**, 1469–1481 (2009).
37. Collins, M. et al. Interannual to decadal climate predictability in the North Atlantic: a multimodel-ensemble study. *J. Clim.* **19**, 1195–1203 (2006).
38. Menary, M. B. et al. Aerosol-forced AMOC changes in CMIP6 historical simulations. *Geophys. Res. Lett.* <https://doi.org/10.1029/2020GL088166> (2020).
39. Booth, B. B. B., Dunstone, N. J., Halloran, P. R., Andrews, T. & Bellouin, N. Aerosols implicated as a prime driver of twentieth-century North Atlantic climate variability. *Nature* **484**, 228–232 (2012).
40. Otterå, O. H., Bentsen, M., Drange, H. & Suo, L. External forcing as a metronome for Atlantic multidecadal variability. *Nat. Geosci.* **3**, 688–694 (2010).
41. Clement, A. et al. The Atlantic Multidecadal Oscillation without a role for ocean circulation. *Science* **350**, 320–324 (2015).
42. Ba, J. et al. A multi-model comparison of Atlantic multidecadal variability. *Clim. Dyn.* **43**, 2333–2348 (2014).
43. Delworth, T. L. & Zeng, F. Multicentennial variability of the Atlantic Meridional Overturning Circulation and its climatic influence in a 4000 year simulation of the GFDL CM2.1 climate model. *Geophys. Res. Lett.* <https://doi.org/10.1029/2012GL052107> (2012).
44. Park, W. & Latif, M. Multidecadal and multicentennial variability of the meridional overturning circulation. *Geophys. Res. Lett.* **35**, L22703 (2008).
45. Folland, C. K., Palmer, T. N. & Parker, D. E. Sahel rainfall and worldwide sea temperatures, 1901–85. *Nature* **320**, 602–607 (1986).
46. Hurrell, J. W. Decadal trends in the North Atlantic Oscillation: regional temperatures and precipitation. *Science* **269**, 676–679 (1995).
47. Delworth, T. L. et al. The central role of ocean dynamics in connecting the North Atlantic Oscillation to the extratropical component of the Atlantic Multidecadal Oscillation. *J. Clim.* **30**, 3789–3805 (2017).
48. Mann, M. E., Steinman, B. A. & Miller, S. K. Absence of internal multidecadal and interdecadal oscillations in climate model simulations. *Nat. Commun.* **11**, 49 (2020).
49. Mann, M. E., Steinman, B. A., Brouillette, D. J. & Miller, S. K. Multidecadal climate oscillations during the past millennium driven by volcanic forcing. *Science* **371**, 1014–1019 (2021).
50. Klavans, J. M., Clement, A. C. & Cane, M. A. Variable external forcing obscures the weak relationship between the NAO and North Atlantic multidecadal SST variability. *J. Clim.* **32**, 3847–3864 (2019).
51. Martin, T., Park, W. & Latif, M. Multi-centennial variability controlled by Southern Ocean convection in the Kiel Climate Model. *Clim. Dyn.* **40**, 2005–2022 (2013).
52. Gervais, M., Shaman, J. & Kushnir, Y. Mechanisms governing the development of the North Atlantic warming hole in the CESM-LE future climate simulations. *J. Clim.* **31**, 5927–5946 (2018).
53. Sévellec, F., Fedorov, A. V. & Liu, W. Arctic sea-ice decline weakens the Atlantic Meridional Overturning Circulation. *Nat. Clim. Change* **7**, 604–610 (2017).
54. Drijfhout, S., van Oldenborgh, G. J. & Cimadoribus, A. Is a decline of AMOC causing the warming hole above the North Atlantic in observed and modeled warming patterns? *J. Clim.* **25**, 8373–8379 (2012).
55. Keil, P. et al. Multiple drivers of the North Atlantic warming hole. *Nat. Clim. Change* **10**, 667–671 (2020).
56. Hodson, D. L. R., Robson, J. I. & Sutton, R. T. An anatomy of the cooling of the North Atlantic Ocean in the 1960s and 1970s. *J. Clim.* **27**, 8229–8243 (2014).
57. Cayan, D. R. Latent and sensible heat flux anomalies over the northern oceans: driving the sea surface temperature. *J. Phys. Oceanogr.* **22**, 859–881 (1992).
58. Lorenz, E. N. *Empirical Orthogonal Functions and Statistical Weather Prediction 1* (Massachusetts Institute of Technology Department of Meteorology, 1956).
59. Myhre, G. et al. in *Climate Change 2013: The Physical Science Basis* (eds Stocker, T. F. et al.) 659–740 (IPCC, Cambridge Univ. Press, 2013).
60. Thompson, D. W. J. & Solomon, S. Interpretation of recent Southern Hemisphere climate change. *Science* **296**, 895–899 (2002).
61. Fogt, R. L. & Marshall, G. J. The Southern Annular Mode: variability, trends, and climate impacts across the Southern Hemisphere. *WIREs Clim. Change* <https://doi.org/10.1002/wcc.652> (2020).
62. Park, W. & Latif, M. Ensemble global warming simulations with idealized Antarctic meltwater input. *Clim. Dyn.* **52**, 3223–3239 (2019).
63. Boer, G. J. & Lambert, S. J. Multi-model decadal potential predictability of precipitation and temperature. *Geophys. Res. Lett.* **35**, L05706 (2008).
64. Boer, G. J., Khari, V. V. & Merryfield, W. J. Decadal predictability and forecast skill. *Clim. Dyn.* **41**, 1817–1833 (2013).
65. Menary, M. B. et al. A multimodel comparison of centennial Atlantic Meridional Overturning Circulation variability. *Clim. Dyn.* **38**, 2377–2388 (2012).
66. Latif, M., Martin, T. & Park, W. Southern Ocean sector centennial climate variability and recent decadal trends. *J. Clim.* **26**, 7767–7782 (2013).
67. Zhang, L., Delworth, T. L., Cooke, W. & Yang, X. Natural variability of Southern Ocean convection as a driver of observed climate trends. *Nat. Clim. Change* **9**, 59–65 (2019).
68. Sun, J., Latif, M., Park, W. & Park, T. On the interpretation of the North Atlantic averaged sea surface temperature. *J. Clim.* **33**, 6025–6045 (2020).
69. Roberts, C. D., Garry, F. K. & Jackson, L. C. A multimodel study of sea surface temperature and subsurface density fingerprints of the Atlantic Meridional Overturning Circulation. *J. Clim.* **26**, 9155–9174 (2013).
70. Drijfhout, S. Competition between global warming and an abrupt collapse of the AMOC in Earth's energy imbalance. *Sci. Rep.* **5**, 14877 (2015).
71. Eyring, V. et al. Overview of the Coupled Model Intercomparison Project phase 6 (CMIP6) experimental design and organization. *Geosci. Model Dev.* **9**, 1937–1958 (2016).
72. Ghan, S. et al. Challenges in constraining anthropogenic aerosol effects on cloud radiative forcing using present-day spatiotemporal variability. *Proc. Natl Acad. Sci. USA* **113**, 5804–5811 (2016).
73. Boucher, O. et al. in *Climate Change 2013: The Physical Science Basis* (eds Stocker, T. F. et al.) 571–658 (IPCC, Cambridge Univ. Press, 2013); <https://doi.org/10.1017/CBO9781107415324.016>
74. Zhang, J. & Zhang, R. On the evolution of Atlantic Meridional Overturning Circulation fingerprint and implications for decadal predictability in the North Atlantic. *Geophys. Res. Lett.* **42**, 5419–5426 (2015).
75. McCarthy, G. D. et al. Sustainable observations of the AMOC: methodology and technology. *Rev. Geophys.* <https://doi.org/10.1029/2019RG000654> (2020).
76. Köhl, A. Evaluation of the GECCO2 ocean synthesis: transports of volume, heat and freshwater in the Atlantic. *Q. J. R. Meteorol. Soc.* **141**, 166–181 (2015).
77. Jackson, L. C. et al. The mean state and variability of the North Atlantic circulation: a perspective from ocean reanalyses. *J. Geophys. Res. Oceans* **124**, 9141–9170 (2019).
78. Danabasoglu, G. et al. North Atlantic simulations in Coordinated Ocean–Ice Reference Experiments phase II (CORE-II). Part II: inter-annual to decadal variability. *Ocean Model.* **97**, 65–90 (2016).
79. Moat, B. I. et al. Pending recovery in the strength of the meridional overturning circulation at 26°N. *Ocean Sci.* **16**, 863–874 (2020).
80. Rossby, T., Chafik, L. & Houpert, L. What can hydrography tell us about the strength of the Nordic Seas MOC over the last 70 to 100 years? *Geophys. Res. Lett.* <https://doi.org/10.1029/2020GL087456> (2020).
81. Zantopp, R., Fischer, J., Visbeck, M. & Karstensen, J. From interannual to decadal: 17 years of boundary current transports at the exit of the Labrador Sea. *J. Geophys. Res. Oceans* **122**, 1724–1748 (2017).
82. Böning, C. W., Behrens, E., Biastoch, A., Getzlaff, K. & Bamber, J. L. Emerging impact of Greenland meltwater on deepwater formation in the North Atlantic Ocean. *Nat. Geosci.* **9**, 523–527 (2016).
83. Gent, P. R. A commentary on the Atlantic Meridional Overturning Circulation stability in climate models. *Ocean Model.* **122**, 57–66 (2018).
84. deYoung, B. et al. An integrated all-Atlantic Ocean observing system in 2030. *Front. Mar. Sci.* **6**, 428 (2019).

Publisher's note Springer Nature remains neutral with regard to jurisdictional claims in published maps and institutional affiliations.



Open Access This article is licensed under a Creative Commons Attribution 4.0 International License, which permits use, sharing, adaptation, distribution and reproduction in any medium or format, as long as you give appropriate credit to the original author(s) and the source, provide a link to the Creative Commons license, and indicate if changes were made. The images or other third party material in this article are included in the article's Creative Commons license, unless indicated otherwise in a credit line to the material. If material is not included in the article's Creative Commons license and your intended use is not permitted by statutory regulation or exceeds the permitted use, you will need to obtain permission directly from the copyright holder. To view a copy of this license, visit <http://creativecommons.org/licenses/by/4.0/>.

© The Author(s) 2022

Methods

Observations. Observed SST during 1900–2019 with $2^\circ \times 2^\circ$ resolution is used here and obtained from Extended Reconstructed Sea Surface Temperature Version 5 (ERSSTv.5; ref. ⁸⁵). SSTs from Kaplan Extended SST v.2 during 1900–2019 with $5^\circ \times 5^\circ$ resolution are also analysed⁸⁶. We use the station-based NAO index from 1900 to 2019 retrieved from <https://climatedataguide.ucar.edu/climate-data/hurrell-north-atlantic-oscillation-nao-index-station-based>. This NAO index is based on the difference in normalized Northern Hemisphere winter (December–March) sea-level pressure between Lisbon, Portugal and Stykkisholmur/Reykjavik, Iceland. The annual-mean NAO index is also used.

Mixed-layer depth climatology with $2^\circ \times 2^\circ$ resolution is from de Boyer Montégut et al.⁸⁷ and based on a density threshold of 0.03 kg m^{-3} .

Annual satellite sea-level data for 1993–2019 are from Copernicus (<https://cds.climate.copernicus.eu>). In the EOF analysis, the Sea Level Anomaly product was used, which is defined relative to the mean of 1993–2012 (ref. ⁸⁸).

Net ERF. Net ERF (expressed in W m^{-2}) is the globally averaged net downward radiative flux at the top of the atmosphere after allowing for atmospheric temperature, water vapour and clouds to adjust but with surface temperature or a portion of surface conditions unchanged¹. The ERF data are from Smith et al.⁸⁹, where they include 14 components: CO_2 , CH_4 , N_2O , other well-mixed GHGs (halogenated compounds), tropospheric O_3 , stratospheric O_3 , stratospheric H_2O , aviation contrails and contrail cirrus, aerosol–radiation interactions, aerosol–cloud interactions, black carbon on snow, land-use change, volcanoes and solar.

In this study, four combinations of the SSPs (SSP1-2.6, SSP2-4.5, SSP3-7.0 and SSP5-8.5)⁹⁰ are used. In Fig. 1d, the combination of the historical ERF due to the CO_2 concentration (1900–2014) and SSP5-8.5 (2015–2019) is shown. The other SSPs are shown in Fig. 2a.

Climate models. An ensemble of 35 historical simulations for 1900–2014 from CMIP6 is used in the calculation of SST indices and S/N-maximizing EOF. The models are: ACCESS-CM2, ACCESS-Earth System Model (ESM) v.1.5, Canadian ESM v.5, CESM2, CESM2-WACCM, CESM2-WACCM-FV2, CIESM, CMCC-CM2-HR4, E3SM-1-0, E3SM-1-1, E3SM-1-1-ECA, FGOALS-f3-L, FGOALS-g3, INM-CM4-8, INM-CM5-0, MIROC6, MPI-ESM-1-2-HAM, MPI-ESM1-2-HR, MPI-ESM1-2-LR, MRI-ESM2-0, NorCPM1, NorESM2-LM, NorESM2-MM, SAM0-UNICON, BCC-CSM2-MR, BCC-ESM1, CAMS-CSM1-0, CAS-ESM2-0, CMCC-CM2-SR5, FIO-ESM2-0, GISS-E2-1G, GISS-E2-1H, IPSL-CM6A-LR and MCM-UA-1-0. Only one ensemble member from each model is used. SST and MOC fields from the first 24 models are used to calculate the combined EOF in Fig. 4. SST and MOC fields are linearly interpolated to $1^\circ \times 1^\circ$ resolution.

EOF analysis. EOF analysis⁵⁸ is a multivariate statistical method. The EOFs are the eigenvectors of the covariance matrix, and they are sorted in descending order by the explained variance. Time series, termed principal components (PCs), are obtained by projecting the original data onto the EOFs. In the joint EOF analysis of the ensemble-mean Atlantic SST and MOC, each variable was normalized by its own field sum of standard deviations, making each field have identical total variance.

POP analysis. POP analysis is a multivariate statistical method and is defined as the normal modes of a linear dynamical representation of the data in terms of a first-order autoregressive-vector process with residual noise forcing^{91–93}. For practical purposes, the original process is usually reduced into the subspace of leading EOFs. Here we use the first 10 EOFs accounting for 90.8% of the total variance.

SST-regression maps. We show global maps of local linear regression coefficients of SST upon the principal components (PCs) that have been normalized by their respective standard deviation. An *F* test is used to assess the significance of the regression coefficients.

S/N-maximizing EOFs. S/N-maximizing EOF analysis refers to a method of identifying the fingerprints of external forcing in an ensemble of forced climate model experiments. The method allows us to distinguish between the response to prescribed external forcing common to all ensemble members and internal variability, which is temporally uncorrelated between ensemble members. We follow the formulation of Venzke et al.⁹⁴. The leading EOF has the largest S/N, and the corresponding PC represents the time evolution of the most dominant forced response.

Significance of correlations. The Student's *t*-test and Monte Carlo simulation based on nonparametric random phase are applied to assess the statistical significance of the correlation coefficients⁹⁵. All correlation coefficients mentioned in the main text are statistically significant at the 95% confidence level.

Data availability

All the datasets used in this study are publicly available: ERSSTv.5 data at <https://psl.noaa.gov/data/gridded/data.noaa.ersst.v5.html>; Kaplan Extended SST v.2 data at https://www.psl.noaa.gov/data/gridded/data.kaplan_sst.html; the station-based NAO index at <https://climatedataguide.ucar.edu/climate-data/hurrell-north-atlantic-oscillation-nao-index-station-based>; mixed-layer depth climatology data at <http://www.ifremer.fr/cerweb/deboyer/mld/home.php>; satellite sea-level data at <https://cds.climate.copernicus.eu>; ERF data at <https://doi.org/10.5281/zenodo.4624765>; and all the CMIP6 model data at <https://esgf-node.llnl.gov/projects/cmip6/>.

Code availability

The figures were generated using MATLAB and *m_map* (<https://www.eoas.ubc.ca/~rich/map.html>), where the basemap data (GSHHG, <https://www.ngdc.noaa.gov/mgg/shorelines/gshhs.html>) are used under the GNU Lesser General Public license. All the codes used in the data processing and visualization are available via Figshare at <https://doi.org/10.6084/m9.figshare.19318004>. Other code is available upon request to the corresponding author J.S.

References

- Huang, B. et al. Extended Reconstructed Sea Surface Temperature, version 5 (ERSSTv5): upgrades, validations, and intercomparisons. *J. Clim.* **30**, 8179–8205 (2017).
- Kaplan, A. et al. Analyses of global sea surface temperature 1856–1991. *J. Geophys. Res. Oceans* **103**, 18567–18589 (1998).
- de Boyer Montégut, C. Mixed layer depth over the global ocean: an examination of profile data and a profile-based climatology. *J. Geophys. Res. Oceans* **109**, C12003 (2004).
- Clementi, E. et al. *Mediterranean Sea Analysis and Forecast (CMEMS MED-Currents, EAS5 system) (Version 1)* (Copernicus Monitoring Environment Marine Service, 2021); https://doi.org/10.25423/CMCC/MEDSEA_ANALYSIS_FORECAST_PHY_006_013_EAS5
- Smith, C. J. et al. Energy budget constraints on the time history of aerosol forcing and climate sensitivity. *J. Geophys. Res. Atmos.* <https://doi.org/10.1029/2020JD033622> (2021).
- Riahi, K. et al. The Shared Socioeconomic Pathways and their energy, land use, and greenhouse gas emissions implications: an overview. *Glob. Environ. Change* **42**, 153–168 (2017).
- Hasselmann, K. PIPs and POPs: the reduction of complex dynamical systems using principal interaction and oscillation patterns. *J. Geophys. Res. Atmos.* **93**, 11015–11021 (1988).
- Storch, H., Bruns, T., Fischer-Bruns, I., Hasselmann, K. & von Storch, H. Principal oscillation pattern analysis of the 30- to 60-day oscillation in general circulation model equatorial troposphere. *J. Geophys. Res. Atmos.* **93**, 11022–11036 (1988).
- von Storch, H., Bürger, G., Schnur, R. & von Storch, J.-S. Principal oscillation patterns: a review. *J. Clim.* **8**, 377–400 (1995).
- Venzke, S., Allen, M. R., Sutton, R. T. & Rowell, D. P. The atmospheric response over the North Atlantic to decadal changes in sea surface temperature. *J. Clim.* **12**, 2562–2584 (1999).
- Ebisuzaki, W. A method to estimate the statistical significance of a correlation when the data are serially correlated. *J. Clim.* **10**, 2147–2153 (1997).

Acknowledgements

J.S. was supported by a PhD scholarship funded jointly by the China Scholarship Council (CSC, no. 201606330057). M.L. was supported by the Roadmap Project funded by the German Ministry of Education and Research (BMBF) (01LP2002C). M.L. and M.V. were supported by the project RACE, funded by the German Ministry of Education and Research (BMBF) (03F0824C). We acknowledge the World Climate Research Program's Working Group on Coupled Modelling, which is responsible for CMIP, and we thank the climate modelling groups for producing and making available their model outputs. For CMIP, the US Department of Energy's Program for Climate Model Diagnosis and Intercomparison provides coordinating support and led development of software infrastructure in partnership with the Global Organization for Earth System Science Portals. This study has been conducted using EU Copernicus Marine Service information.

Author contributions

M.L. conceived the study and led the discussion and the writing of the first draft of the manuscript. J.S. performed the analysis and produced all the figures in the main text and seven Extended Data figures. M.H.B. and J.S. together produced one Extended Data figure. J.S., M.V. and M.H.B. contributed to improving the manuscript. All authors contributed to the methods design, results analysis and manuscript reviewing.

Funding

Open access funding provided by GEOMAR Helmholtz-Zentrum für Ozeanforschung Kiel.

Competing interests

The authors declare no competing interests.

Additional information

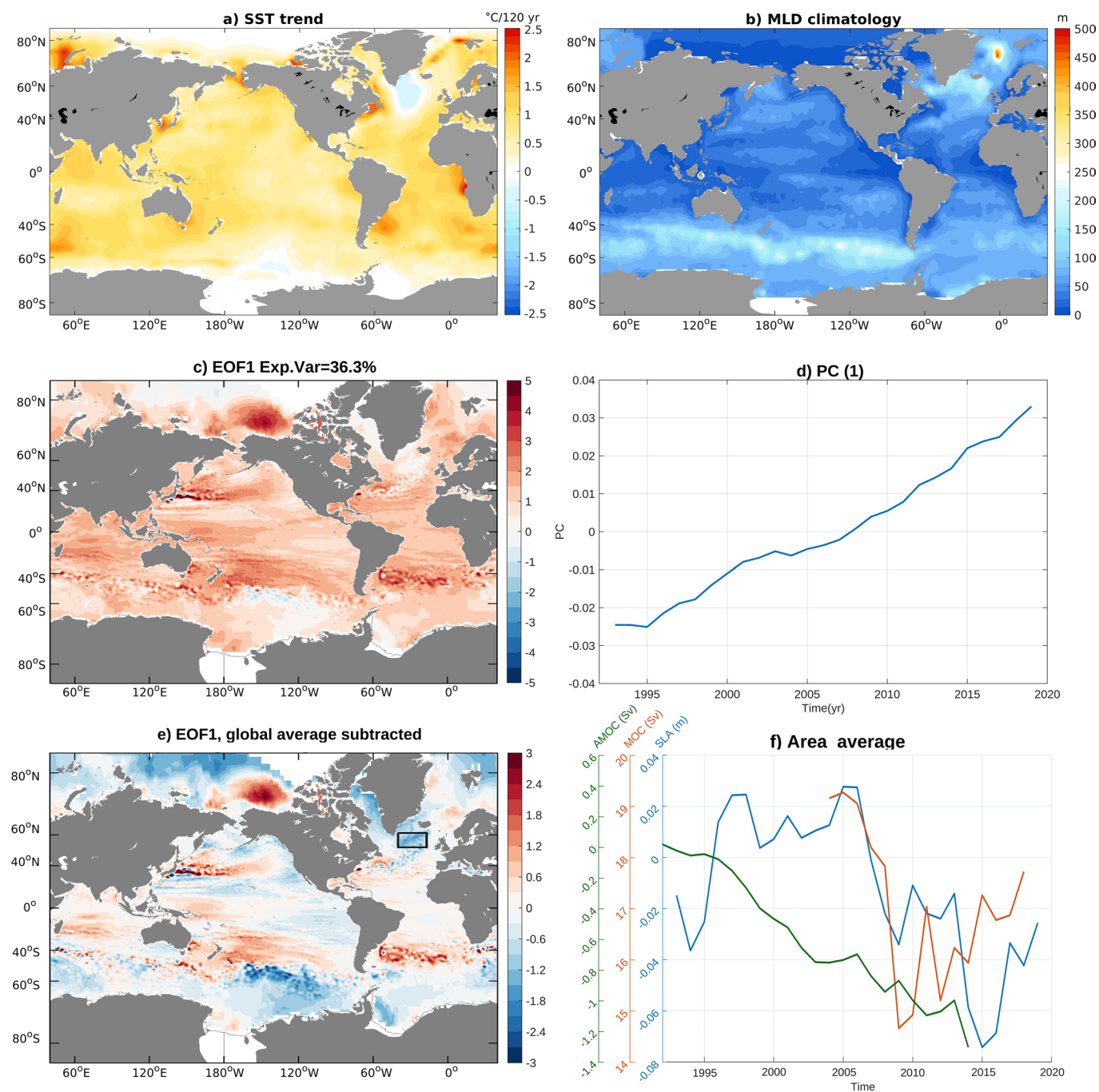
Extended data is available for this paper at <https://doi.org/10.1038/s41558-022-01342-4>.

Supplementary information The online version contains supplementary material available at <https://doi.org/10.1038/s41558-022-01342-4>.

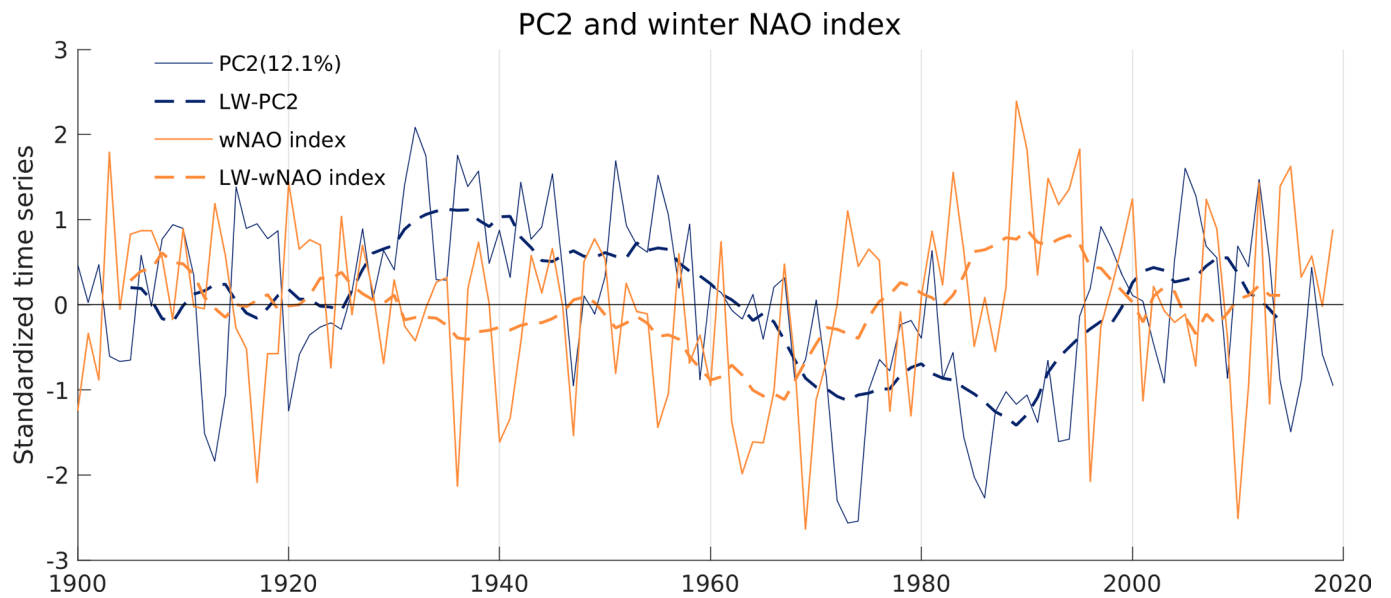
Correspondence and requests for materials should be addressed to Mojib Latif or Jing Sun.

Peer review information *Nature Climate Change* thanks Emma Worthington and the other, anonymous, reviewer(s) for their contribution to the peer review of this work.

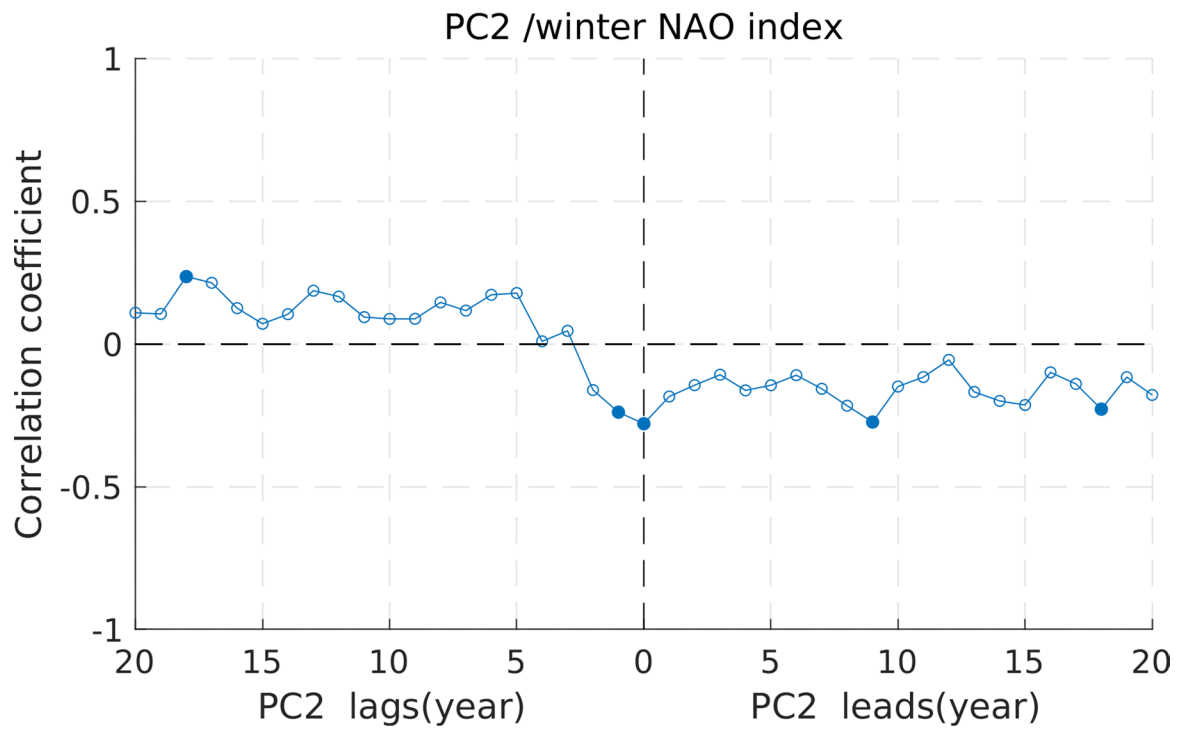
Reprints and permissions information is available at www.nature.com/reprints.



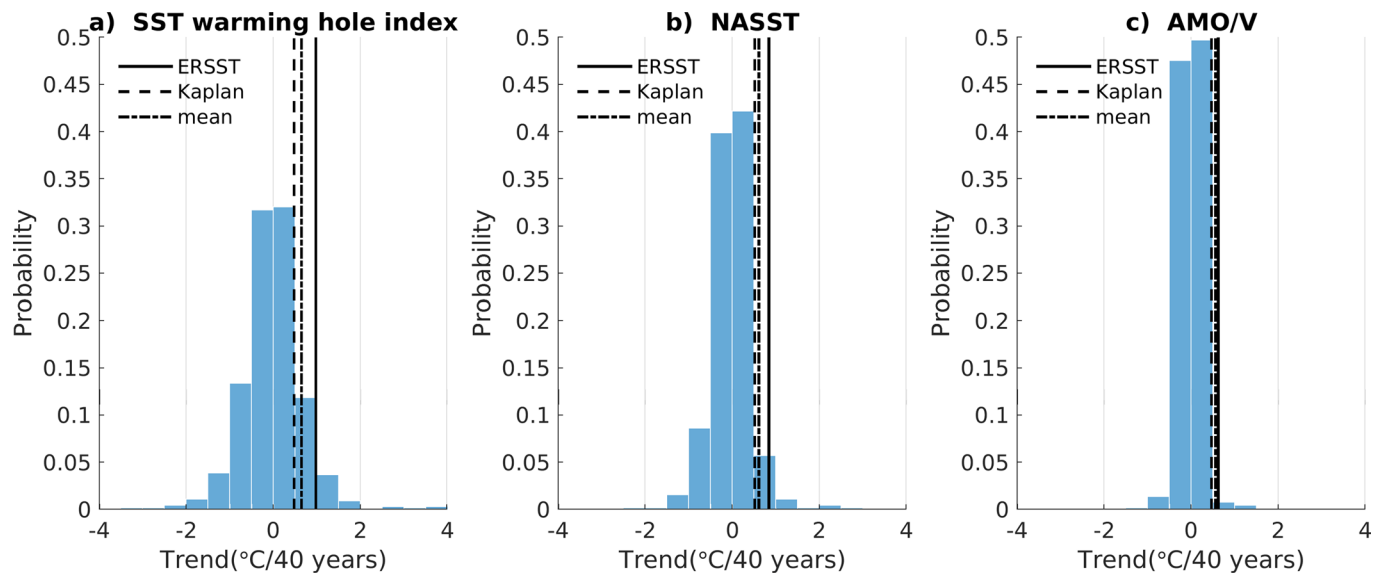
Extended Data Fig. 1 | Climatology and SL EOF. Extended Data Fig. 1 **a**) Map of the linear trends 1900–2019 of observed sea surface temperature (SST, °C/120 years). **b**) Mean mixed layer depth (MLD, m) from observations and averaged over 1961–2008. The criterion for defining MLD is based on a fixed threshold of 0.03 kg/m^3 . **c**) Leading EOF mode of sea-level variability (EOF1_{SL} , m), calculated over the period 1993–2019. EOF1_{SL} accounts for 36.3% of the total sea-level variance. **d**) The corresponding principal component time series (PC1_{SL}) of EOF1. **e**) As c), but with the global average removed (dynamic sea level linked to EOF1_{SL}). The globally averaged trend in annual-mean sea level during 1993–2019 amounts to 2.86 mm/year . **f**) Time series of EOF1_{SL} -related dynamic sea level (m, blue curve) averaged over the box southeast of Greenland (40°W – 17°W , 53°N – 61°N), which is shown in e). Superimposed are the overturning (Sv) data 2004–2018 from the RAPID array at 26.5°N (orange curve) and the AMOC index 1993–2014 at 26.5°N (green curve) that has been reconstructed from the joint (SST, MOC) EOF1_{mod} calculated from the historical simulations with the CMIP6 models (Fig. 4).



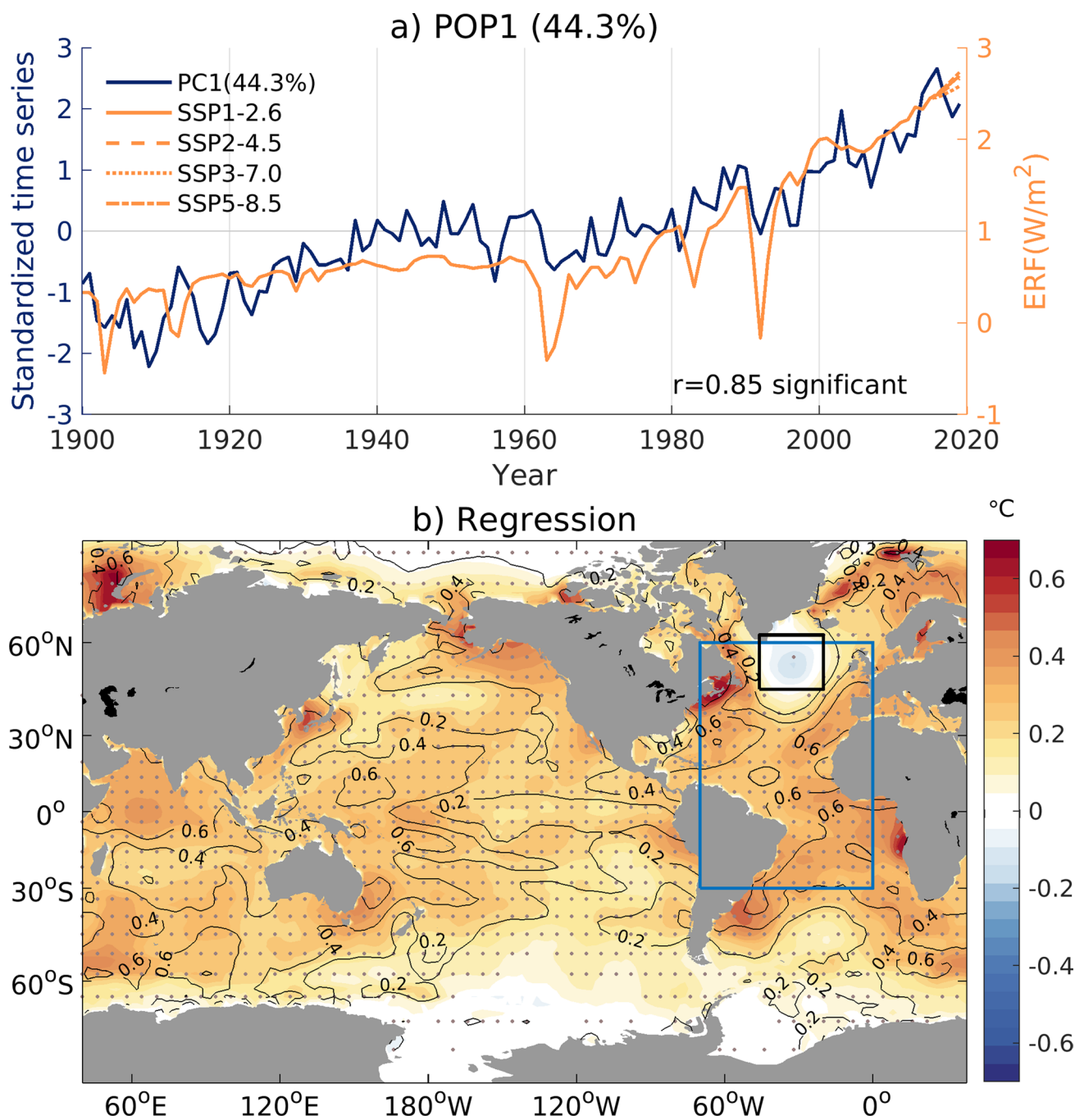
Extended Data Fig. 2 | PC2 and NAO index. Extended Data Fig. 2 PC2 (thin blue curve) of EOF2 and the winter-NAO index (December to February, station-based, thin orange curve). Dashed thick curves indicate the low-pass (LW) filtered indices, PC2 (blue lines), winter-NAO index (orange lines).



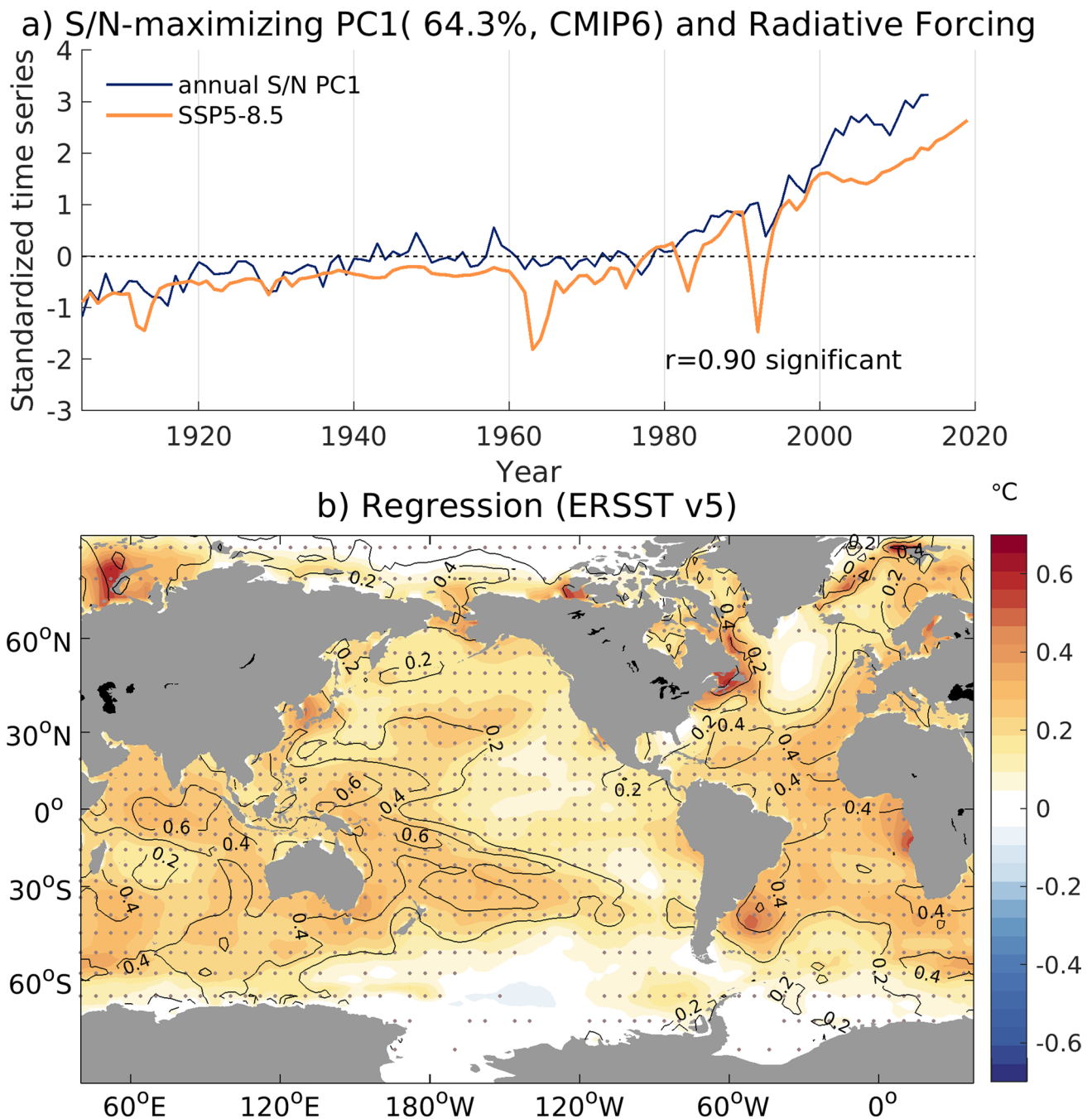
Extended Data Fig. 3 | Cross correlation between PC2 and NAO index. Extended Data Fig. 3 Cross-correlation function as a function of the time lag coefficient between PC2 and winter-NAO index. Filled dots indicate significance at the 95% confidence level.



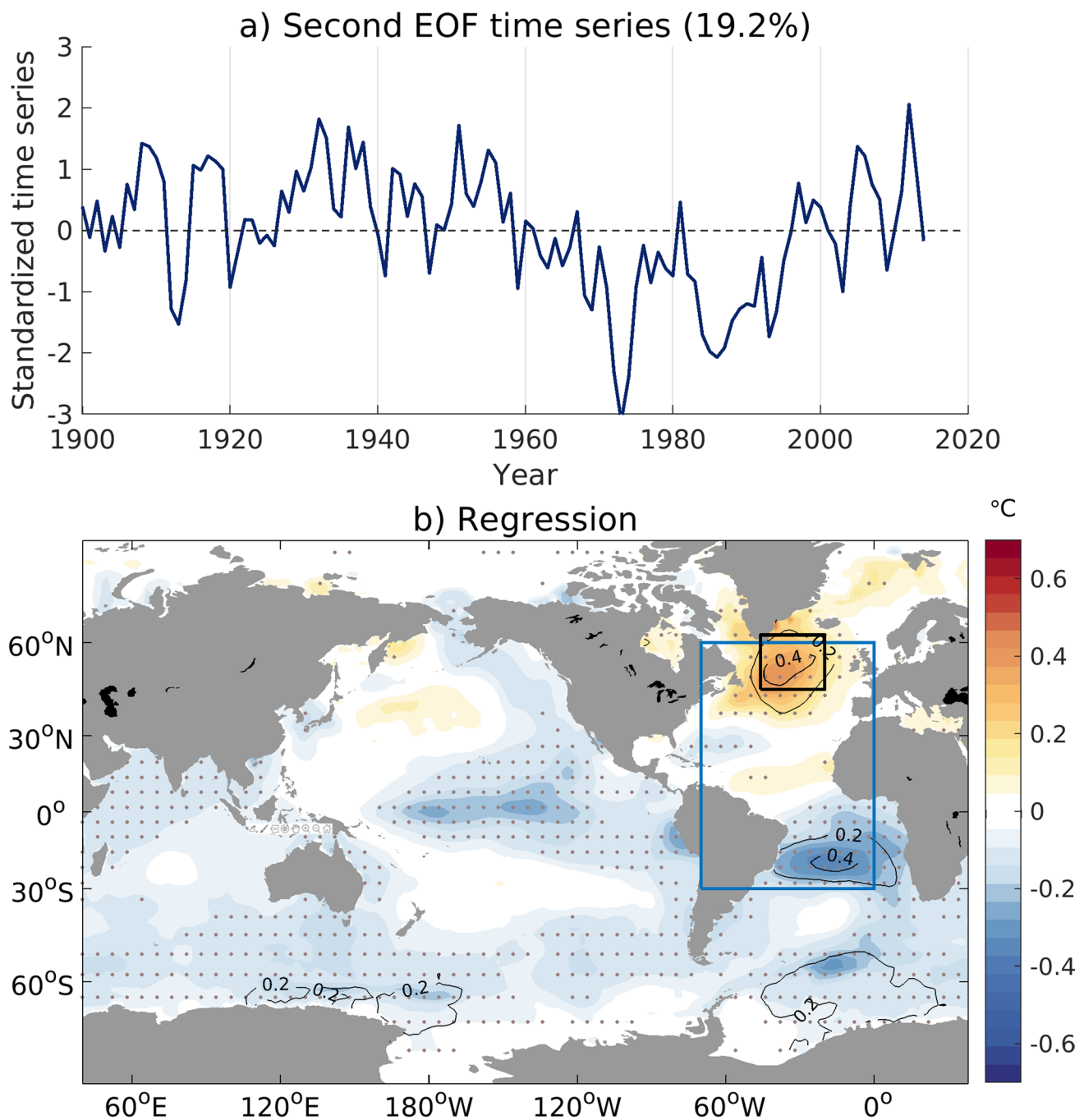
Extended Data Fig. 4 | Distribution of 40-year SST trend. Extended Data Fig. 4 Probability distribution of non-overlapping 40-year SST trends in the regions of the three SST indices (with an interval of 0.5°C/40 years), derived from the control integrations of the CMIP6 models. Vertical black solid line indicates the 40-year trend from ERSST (1975–2014), vertical black dashed line indicates Kaplan SST (1975–2014), vertical black dashed-dotted line indicates ensemble mean of the historical CMIP6 models (1975–2014).



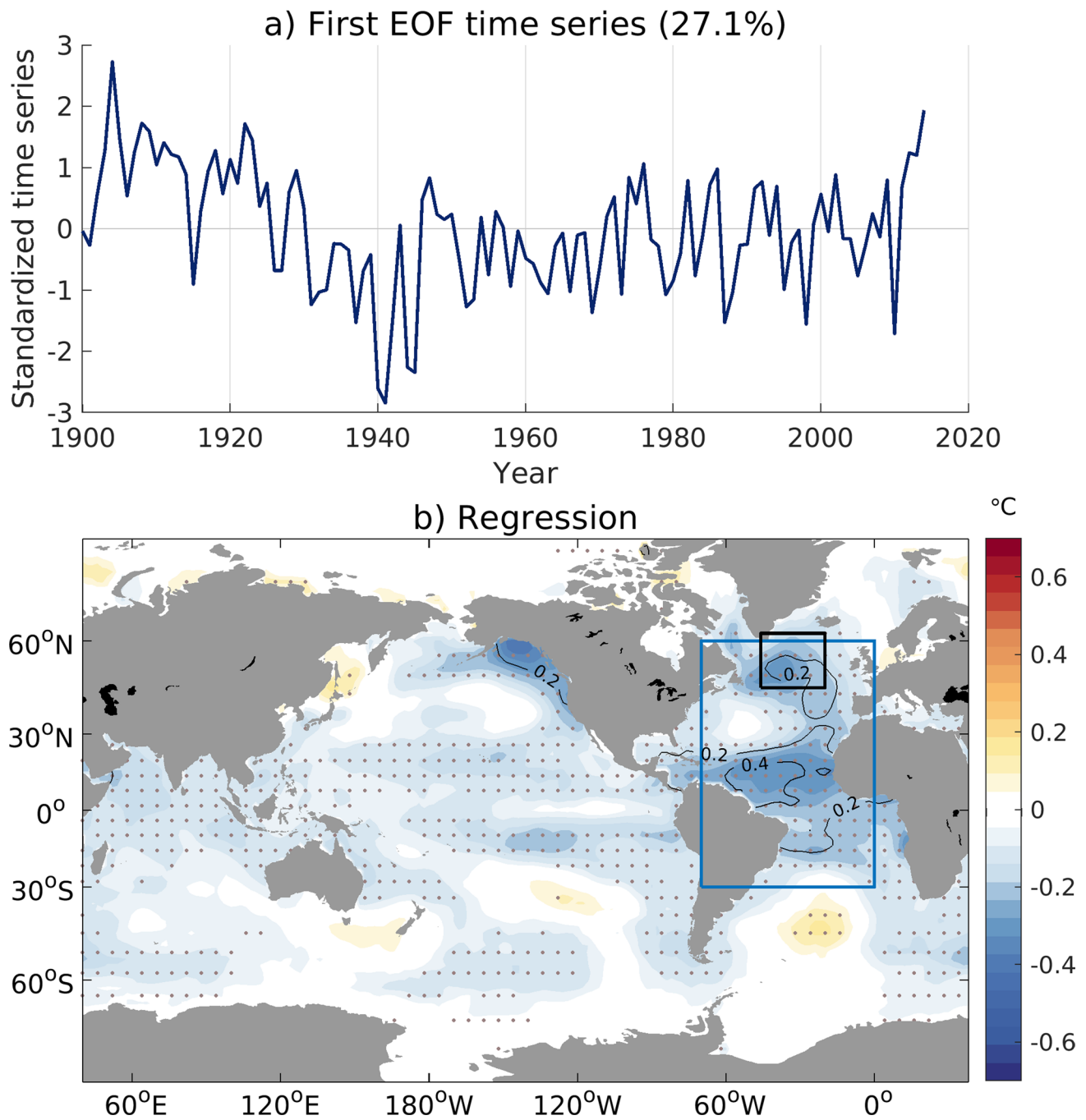
Extended Data Fig. 5 | POP1 timeseries and regression map. Extended Data Fig. 5 Leading (most energetic) Principal Oscillation Pattern mode (POP1), accounting for 44.3% of the total Atlantic SST variability. a) Standardized POP coefficient time series of POP1 (PC1, blue) and the net effective radiative forcing (ERF; W/m^2 , orange) with different scenarios after 2014 (SSP1-2.6, SSP2-4.5, SSP3-7.0 and SSP5-8.5). PC1 and ERF with SSP5-8.5 are correlated at 0.85, which is significant at the 95% confidence level. b) POP1 pattern shown by the local regression coefficients ($^{\circ}C$) of the observed SSTs (ERSST_v5) upon PC1. The contours denote the explained variance, the contour interval is 0.2, and the dots indicate significance at the 95% level.



Extended Data Fig. 6 | S/N maximizing EOF1 timeseries and regression map. Extended Data Fig. 6 Leading signal-to-noise ratio maximizing Empirical Orthogonal Function (S/N-EOF1) calculated from the historical simulations (1850 to 2014) with the CMIP6 models. a) The principal component time series (S/N-PC1, blue) of S/N-EOF1 and the standardized historical ERF (orange, with SSP5-8.5 pathway at the end). The correlation coefficient between the PC1 and ERF is 0.9, which is significant at 95% confidence level. b) Map of local regression coefficients (°C) of the observed SSTs (ERSST_v5) upon S/N-PC1. The contours denote the explained variance, the contour interval is 0.2, and the dots indicate significance at the 95% level.



Extended Data Fig. 7 | EOF2 timeseries and regression map of residual SST. Extended Data Fig. 7 Second most energetic EOF mode (EOF2_{res}) after removing the leading signal-to-noise ratio maximizing Empirical Orthogonal Function (S/N-EOF1, Extended Data Fig. 6) calculated from the historical simulations with the CMIP6 models. a) The corresponding principal component time series (PC2_{res}). b) Map of local regression coefficients ($^{\circ}\text{C}$) of the observed SSTs (ERSST_v5) upon PC2_{res} . The contours denote the explained variance, the contour interval is 0.2, and the dots indicate significance at the 95% level.



Extended Data Fig. 8 | EOF1 timeseries and regression map of residual SS. Extended Data Fig. 8 Leading EOF mode ($EOF1_{res}$) after removing the leading signal-to-noise ratio maximizing Empirical Orthogonal Function (S/N-EOF1 (Extended Data Fig. 6) calculated from the historical simulations with the CMIP6 models. a) The corresponding principal component time series ($PC1_{res}$). b) Map of local regression coefficients ($^{\circ}\text{C}$) of the observed SSTs (ERSST_v5) upon $PC1_{res}$. The contours denote the explained variance, the contour interval is 0.2, and the dots indicate significance at the 95% level.